OPTICA

Doubly resonant metal-free electro-optic microwave receiver in aluminum nitride

STEVEN T. LIPKOWITZ,[1,*] WARREN P. BERK,[2] KAREN E. GRUTTER,[1,2] AND THOMAS E. MURPHY[1,3]

[1]University of Maryland, Department of Electrical and Computer Engineering, 8223 Paint Branch Drive, College Park, Maryland 20742, USA
[2]Laboratory for Physical Sciences, 8050 Greenmead Drive, College Park, Maryland 20740, USA
[3]University of Maryland, Institute for Research in Electronics and Applied Physics, 8279 Paint Branch Drive, College Park, Maryland 20742, USA
*STL@terpmail.umd.edu

Received 2 October 2023; revised 11 April 2024; accepted 23 April 2024; published 17 May 2024

This paper demonstrates a passive, integrated electro-optic receiver for detection of free-space microwave radiation. Unlike a traditional microwave receiver, which relies on conductive antennas and electrical amplifiers, this receiver uses only passive, optically probed elements with no electrodes or electronic components. The receiver employs two co-resonant structures: a dielectric resonator antenna (DRA) to concentrate incoming microwave radiation and an integrated aluminum nitride (AlN) racetrack resonator to resonantly enhance the optical carrier. The microwave field of the DRA modulates the built-up optical carrier in the resonator via the electro-optic response of AlN. We successfully detected 15 GHz microwave radiation through co-resonant electro-optic up-conversion, without the need for any conducting electrodes, amplifiers, or electronic components.

https://doi.org/10.1364/OPTICA.507320

1. INTRODUCTION

Microwave and millimeter-wave signal detection is required in various applications, including automotive radar, security screening, radio astronomy, satellite and wireless communication, and quantum computing [1–6]. Traditional microwave receivers use antennas, amplifiers, mixers, or rectifiers to convert the microwave signal to a detectable baseband signal. In some cases, it is desirable to up-convert the microwave signal onto an optical carrier, where it can be more easily transmitted, processed, and measured via photodetection [7]. While photonic components are smaller, lighter, and consume less power than their microwave counterparts, the transduction of a propagating microwave plane wave onto a guided optical carrier typically requires an antenna, electrical amplifier, and travelling-wave electro-optic modulator, which are difficult to integrate in a single chip-scale device. Additionally, the electrical amplifier and bulk fiber-optic components are power-hungry devices, and significant efficiency gains could be achieved by integrating the microwave antenna structure and electro-optic modulator into a single photonic integrated circuit. Electro-optic modulators with on-chip integrated antennas have been reported utilizing a variety of electro-optic materials and antenna structures [8–15]. However, these devices all employ small conducting antenna elements, and conductive losses in these antenna structures impose significant limitations on performance as microwave frequencies increase. While on-chip metal-free electro-optic modulator designs have been reported [16], these devices lack any sort of antenna structure to enhance incident microwave fields. Dielectric resonator antenna (DRA) structures are an attractive alternative to traditional conducting antennas, as they are nearly unaffected by conductive losses at these higher frequencies and are made of a material with a high relative permittivity (ϵ_r), which allows for a significantly smaller footprint than their conducting counterparts [17]. Additionally, DRA structures are immune to damage from electromagnetic interference effects and electrostatic discharge, which are significant risks for conventional microwave antenna and amplifier structures, especially at higher frequencies where protective components can significantly limit performance [18,19].

Others have demonstrated that incorporating optical resonant structures into electro-optic modulator designs can increase modulation efficiency and reduce device footprint due to the large buildup of optical fields under resonant conditions [20,21]. Additional inclusion of a microwave resonant structure can allow for a similar buildup of microwave fields and thus further improve modulation efficiency, which has been demonstrated by coupling an external microwave resonator to an optical resonator [22,23] and by designing the optical resonator to support both optical and microwave modes [24]. DRA-coupled electro-optic modulators operating at microwave frequencies have also been demonstrated [25–27]; however, on-chip integration of these designs has yet to be investigated.

Here, to the best of our knowledge, for the first time, we present an entirely metal-free on-chip doubly resonant microwave receiver consisting of an integrated AlN racetrack optical resonator and a microwave frequency DRA. In our design, the DRA concentrates and enhances the electric field from incident microwave radiation,

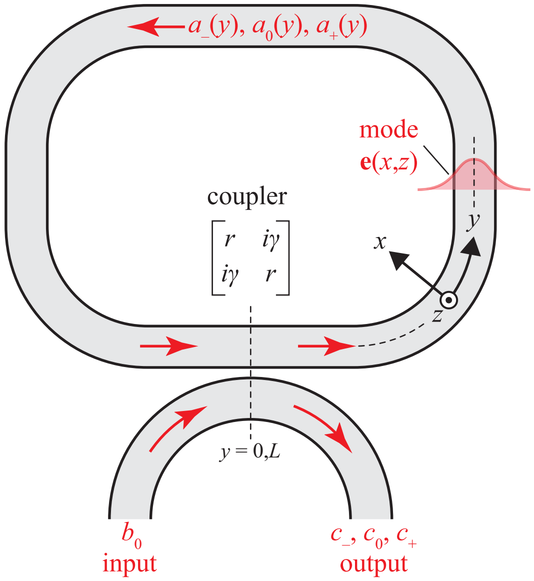

Fig. 1. To analyze the electro-optic resonator, we adopt a coordinate system where y denotes the propagation distance (from 0 to L) measured along the path of the racetrack resonator, and x and z are the local in-plane and out-of-plane transverse coordinates, respectively. A directional coupler at $y = 0$ couples a continuous input wave of amplitude b_0 into the resonator and extracts a portion of the modulated fields.

while the AlN racetrack allows for localized buildup of the optical carrier. By placing the AlN racetrack in proximity to the DRA resonant mode, the enhanced microwave electric field is able to directly modulate the optical carrier via the Pockels effect in a passive AlN optical waveguide. Using this design, we were able to up-convert the microwave signal to an optical carrier without the need for any conducting electrodes, antenna elements, or electrical amplification.

2. ELECTRO-OPTIC OPTICAL RESONATOR THEORY

To understand the performance of our device, we must also understand how light in an electro-optic resonator interacts with an external electric field. The optical field traveling in the racetrack is described by

$$\mathbf{E}(x, y, z, t) = \frac{1}{2}\mathbf{e}(x, z)A(y, t)e^{i[(\beta_0+i\alpha)y-\omega_0 t]} + \text{c.c.}, \quad (1)$$

where $\mathbf{e}(x, z)$ and $\mathbf{h}(x, z)$ (not shown) describe the mode of the waveguide, β_0 is the propagation constant at the optical carrier frequency ω_0, α is the field attenuation factor, and $A(y, t)$ is a slowly varying envelope. For the resonator considered here, y is a generalized coordinate measured along the path of the waveguide, and x and z are the local in-plane and out-of-plane transverse coordinates, respectively, as illustrated in Fig. 1. The z-axis coincides with the crystal axis of the AlN films used here, and it is also the direction from which the microwave signal is incident.

In the absence of an electro-optic effect, and ignoring group velocity dispersion, the envelope $A(y, t)$ evolves according to

$$\frac{\partial}{\partial y}A(y, t) + \beta_1\frac{\partial}{\partial t}A(y, t) = 0, \quad \beta_1 \equiv \left.\frac{\partial\beta}{\partial\omega}\right|_{\omega_0} = \frac{1}{v_g}, \quad (2)$$

which has the solution $A(y, t) = A(0, t - \beta_1 y)$, i.e., a modulation envelope traveling at the group velocity, v_g.

When an external electric field $\mathbf{E}^{\text{ext}}(x, y, z, t)$ is present, the wave acquires a phase modulation through the linear electro-optic effect, which modifies the envelope equation:

$$\frac{\partial}{\partial y}A(y, t) + \beta_1\frac{\partial}{\partial t}A(y, t) = i\Delta\beta(y, t)A(y, t), \quad (3)$$

where $\Delta\beta$ is a local change in the propagation constant, given by

$$\Delta\beta(y, t) \equiv -\frac{\omega_0}{c} \times \frac{\iint r_{jkl}n_j^2 n_k^2 e_j^*(x, z)e_k(x, z)E_l^{\text{ext}}(x, y, z, t)\text{d}x\text{d}z}{\sqrt{\frac{\mu_0}{\epsilon_0}}\iint\left[\mathbf{e}(x, z)\times\mathbf{h}^*(x, z) + \mathbf{e}^*(x, z)\times\mathbf{h}(x, z)\right]\cdot\hat{y}\text{d}x\text{d}z}. \quad (4)$$

Here $r_{jkl}(x, z)$ is the electro-optic tensor, $n_j(x, z)$ is the refractive index along the jth Cartesian direction, and the numerator includes an implied summation over the three Cartesian indices (j, k, l).

A sinusoidally varying field at frequency Ω can be represented by

$$\mathbf{E}^{\text{ext}}(x, y, z, t) = \frac{1}{2}\hat{E}^{\text{RF}}(x, y, z)e^{-i\Omega t} + \text{c.c.}, \quad (5)$$

where $\hat{E}^{\text{RF}}(x, y, z)$ is a complex phasor describing the amplitude, direction, and phase of the external field at each position. For this case, (3) can be directly integrated (after translating to a reference frame moving at the group velocity) to give the envelope after one full round trip:

$$A(L, t) = A(0, t - \beta_1 L)\exp\left[i\left(\frac{m}{2}e^{-i\Omega t} + \text{c.c.}\right)\right], \quad (6)$$

where the modulation amplitude m is

$$m = -\frac{\omega_0}{c}\frac{\oint\iint r_{jkl}n_j^2 n_k^2 e_j^*(x, z)e_k(x, z)\hat{E}_l^{\text{RF}}(x, y, z)e^{i\Omega\beta_1(L-y)}\text{d}x\text{d}z\text{d}y}{\sqrt{\frac{\mu_0}{\epsilon_0}}\iint\left[\mathbf{e}(x, z)\times\mathbf{h}^*(x, z) + \mathbf{e}^*(x, z)\times\mathbf{h}(x, z)\right]\cdot\hat{y}\text{d}x\text{d}z}. \quad (7)$$

Aluminum nitride is a uniaxial crystal of the 6 mm symmetry group, which has an electro-optic tensor of the form

$$\mathbf{r} = \begin{bmatrix} \cdot & \cdot & r_{13} \\ \cdot & \cdot & r_{13} \\ \cdot & \cdot & r_{33} \\ \cdot & r_{42} & \cdot \\ r_{42} & \cdot & \cdot \\ \cdot & \cdot & \cdot \end{bmatrix}, \quad (8)$$

which is rotationally invariant about the z-axis. Because r_{42} is small in comparison to r_{13} and r_{33}, efficient electro-optic modulation requires that the external applied field be oriented along the z-axis of the crystal. For the x-polarized TE mode, with a z-oriented applied field, the round-trip modulation amplitude simplifies to

$$m = -\frac{\pi r_{13}n_o^4}{\lambda n_{\text{eff}}}\frac{\oint\iint_{\text{core}}|\Psi(x, z)|^2\hat{E}_z^{\text{RF}}(x, y, z)e^{i\Omega\beta_1(L-y)}\text{d}x\text{d}z\text{d}y}{\iint|\Psi(x, z)|^2\text{d}x\text{d}z}, \quad (9)$$

where $\Psi(x, z)$ is the quasi-TE mode profile, n_{eff} is the effective refractive index of the optical mode in the racetrack, n_o is the ordinary refractive index of AlN, and $\lambda = 2\pi c/\omega_0$ is the vacuum wavelength. The integral in the numerator is taken only over the aluminum nitride core, and over a closed interval spanning one full round trip from $y = 0$ to L. In the case that $2\pi/\Omega = \beta_1 L$, the modulation amplitude would average to zero for any $E_z^{\mathrm{RF}}(x, y, z)$ that is uniform in y.

When $|m| \ll 1$, we can ignore all but the $\pm\Omega$ modulation sidebands:

$$A(y, t) = a_-(y)e^{i\Omega t} + a_0(y) + a_+(y)e^{-i\Omega t}. \tag{10}$$

Substituting (10) into (6) and expanding to first order in m, we obtain the spectral components after one round trip:

$$\begin{aligned} a_-(L) &= \left[e^{-i\Omega\beta_1 L}a_-(0) + i\frac{m^*}{2}a_0(0)\right] \\ a_+(L) &= \left[e^{+i\Omega\beta_1 L}a_+(0) + i\frac{m}{2}a_0(0)\right] \\ a_0(L) &= a_0(0). \end{aligned} \tag{11}$$

To complete the analysis, we introduce a directional coupler at $y = 0$ that couples a continuous input wave of amplitude b_0 into the resonator and extracts a portion of the modulated fields. The 2×2 directional coupler applies separately to each of the three spectral components:

$$\begin{bmatrix} a_-(0) \\ c_- \\ a_0(0) \\ c_0 \\ a_+(0) \\ c_+ \end{bmatrix} = \left[\begin{array}{cc|cc|cc} r & i\gamma & \cdot & \cdot & \cdot & \cdot \\ i\gamma & r & \cdot & \cdot & \cdot & \cdot \\ \hline \cdot & \cdot & r & i\gamma & \cdot & \cdot \\ \cdot & \cdot & i\gamma & r & \cdot & \cdot \\ \hline \cdot & \cdot & \cdot & \cdot & r & i\gamma \\ \cdot & \cdot & \cdot & \cdot & i\gamma & r \end{array}\right] \begin{bmatrix} a_-(L)e^{i\beta_0 L}e^{-\alpha L} \\ 0 \\ a_0(L)e^{i\beta_0 L}e^{-\alpha L} \\ b_0 \\ a_+(L)e^{i\beta_0 L}e^{-\alpha L} \\ 0 \end{bmatrix}, \tag{12}$$

where $r^2 + \gamma^2 = 1$, and the factor $e^{i\beta_0 L}e^{-\alpha L}$ accounts for the phase delay and attenuation occurring in one round trip.

Eqs. (11) and (12) can be directly solved for the three output spectral amplitudes:

$$c_0 = \left(\frac{r - e^{i\beta_0 L}e^{-\alpha L}}{1 - re^{i\beta_0 L}e^{-\alpha L}}\right) b_0, \tag{13}$$

$$c_- = -i\frac{m^*}{2}\frac{(1 - r^2)e^{i\beta_0 L}e^{-\alpha L}}{\left(1 - re^{i\beta_0 L}e^{-\alpha L}\right)\left(1 - re^{i\beta_- L}e^{-\alpha L}\right)}b_0, \tag{14}$$

$$c_+ = -i\frac{m}{2}\frac{(1 - r^2)e^{i\beta_0 L}e^{-\alpha L}}{\left(1 - re^{i\beta_0 L}e^{-\alpha L}\right)\left(1 - re^{i\beta_+ L}e^{-\alpha L}\right)}b_0, \tag{15}$$

where $\beta_\pm \equiv \beta_0 \pm \beta_1\Omega$ is the propagation constant for the upper and lower spectral sidebands.

Eq. (13) describes the conventional transmission spectrum of a racetrack resonator, which shows periodic dips in transmission when the input frequency is tuned to a resonance, i.e., when $\beta_0 L = 2\pi n$. The modulation sidebands (14) and (15) scale in proportion to $|m|$, as expected, but they also exhibit a resonant enhancement when both $\beta_0 L = 2\pi n$ and $\beta_\pm L = 2\pi(n \pm 1)$. The latter condition is satisfied when $2\pi/\Omega = \beta_1 L$, meaning that temporal period of the sinusoidal modulation matches the round-trip group delay of the resonator, i.e. when the microwave frequency matches the optical resonator free spectral range (FSR). Under this resonant condition, the sideband spectral power is

$$|c_\pm|^2 = \frac{|m|^2}{4}\left[\frac{1 - r^2}{(1 - re^{-\alpha L})^2}\right]^2 e^{-2\alpha L}|b_0|^2. \tag{16}$$

The factor in square brackets is maximized by choosing $r = e^{-\alpha L}$, which corresponds to critical coupling. Under this condition, the transmitted carrier c_0 is suppressed, and the sideband power is proportional to the square of the finesse F:

$$|c_\pm|^2 = \frac{|m|^2 F^2}{4\pi^2}|b_0|^2, \qquad F \equiv \frac{\pi e^{-\alpha L}}{1 - e^{-2\alpha L}}. \tag{17}$$

3. MICROWAVE RESONATOR

The dielectric antenna in our design uses the fundamental $\mathrm{TE}_{01\delta}$ mode of a high permittivity ($\epsilon_R = 78$) cylinder with a 1 mm radius and length of 4 mm, which has a resonant frequency of approximately 15 GHz. The loss tangent of the dielectric material at 15 GHz is 1.875×10^{-3} and is presumed to scale linearly with frequency. The $\mathrm{TE}_{01\delta}$ microwave resonance exhibits an azimuthal electric field inside of the dielectric cylinder, and a far-field radiation pattern that matches that of a magnetic dipole oriented along the cylinder axis [17]. Accordingly, the $\mathrm{TE}_{01\delta}$ mode can be best excited by any plane wave incident in the equatorial plane of the cylinder and polarized perpendicular to the cylinder axis. The microwave resonant frequency and quality factor depend primarily on the permittivity and aspect ratio, and they can be engineered using well-established semi-analytical formulas [17] or through direct numerical simulation. The resonant field amplitude is strongest in the interior of the dielectric, and it decays evanescently outside of the cylinder. To best exploit this enhancement, we introduce a ground plane that bisects the cylinder along an axial plane, which produces a resonant oscillating electric field pointing normal to ground plane. The optical resonator is then incorporated into a thin-film electro-optic waveguide fabricated above the ground plane and below the DRA, as shown schematically in Fig. 2(a). In this free-space-coupled configuration, radiation is the dominant source of loss for the DRA resonant mode, and the small amount of DRA material loss can be neglected by comparison.

Figures 2(b) and 2(d) show the electric fields of the DRA resonant mode, simulated using a finite element method (FEM) eigenfrequency solver. The resonant fields at the DRA-substrate interface are perpendicular to the substrate, which is the desired configuration for many electro-optic thin films, including the aluminum nitride used here. Additionally, the field changes polarity between the two halves of the DRA, which ensures that when the electro-optic racetrack resonator is placed beneath the dielectric, the cumulative electro-optic modulation amplitude (9) does not integrate to zero through one round trip when the microwave frequency is matched to the optical resonator FSR. This matching is necessary to maximize the electro-optic modulation in the optical resonator, as discussed in detail in Section 2.

On resonance, the magnitude of the z-directed electric field beneath the DRA can be orders of magnitude stronger than the incident electric field. However, FEM simulations of the millimeter-scale dielectric resonator cannot easily incorporate the sub-micron-scale aluminum nitride waveguide, which makes it difficult to directly simulate the microwave field amplitude inside of the waveguide, where the electro-optic modulation occurs. Moreover, the fields at the ground plane are vertically oriented and therefore experience a discontinuity at each horizontal interface. Because the SiO_2 and AlN films that make up the optical device layer are thin compared to the microwave wavelength, and because the aluminum nitride waveguide has a low aspect ratio, one can approximate the vertical electric fields in each region using the

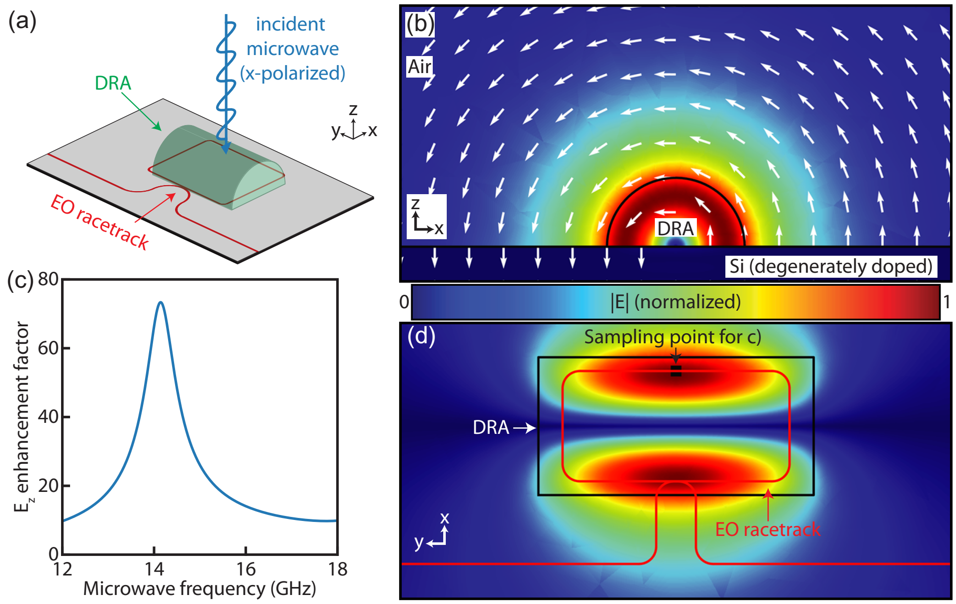

Fig. 2. (a) Schematic of device design showing a DRA sitting atop an on-chip electro-optic (EO) racetrack resonator. (b) Simulated normalized electric field magnitude ($|E|$) on resonance in a cross section through the equatorial plane of the DRA. The white arrows indicate the direction of E. The electro-optic waveguides are located within an optical device layer between the Si and the DRA and are not included due to scale. (c) Electric field z-component enhancement $|E_z(\mathrm{AlN})|/|E_{\mathrm{in}}|$ as a function of microwave frequency when the DRA is excited from the out-of-plane direction by an x-polarized plane wave. The simulated electric field just inside the DRA is sampled at a point above where the AlN racetrack intersects the equatorial plane of the DRA, as shown in (d). The electric field in the AlN is then calculated via (18). (d) Top-down view of the DRA showing the normalized electric field magnitude ($|E|$) on resonance in the plane coinciding with the bottom of the DRA. A schematic of the optical racetrack is superimposed, as is the sampling point described in (c). Simulations in (b) and (d) performed using FEM eigenmode solver. Simulation in (c) performed using FEM frequency domain solver.

quasi-electrostatic assumption that $D_z \equiv \epsilon E_z$ is homogeneous in the vicinity of the surface. The field E_z in the AlN film can then be estimated from the field just inside the dielectric resonator as

$$E_z^{\mathrm{AlN}} = \frac{\epsilon_{\mathrm{DRA}}}{\epsilon_{\mathrm{AlN}}} E_z^{\mathrm{DRA}}. \tag{18}$$

To calculate the electric field in the AlN in the presence of an incident microwave plane wave, we simulate the structure using an FEM frequency domain solver. In this simulation, we include a 6 μm SiO_2 layer between the DRA and Si substrate, which represents the oxide cladding surrounding our AlN devices. Figure 2(c) shows the simulated electric field z-component enhancement $|E_z^{\mathrm{AlN}}|/|E_{\mathrm{in}}|$ as a function of microwave frequency when the DRA is excited from the out-of-plane direction by an x-polarized plane wave. The simulated electric field just inside the DRA is sampled at a point above where the AlN racetrack intersects equatorial plane of the DRA, as shown in Fig. 2(d). The electric field in the AlN is then calculated via (18). Because the peak electric field enhancement in the AlN increases as the separation between the DRA and ground plane decreases (not shown), we have chosen to use degenerately doped Si as both the ground plane and the substrate for our photonic chip. By using a degenerately doped silicon substrate as both the ground plane and substrate, we minimize the distance between the ground plane and DRA.

To verify the frequency of the DRA mode of interest, we perform reflection measurements as shown in Fig. 3(a). A hollow WR-62 waveguide is positioned top down over the DRA and capped by a post-fabrication chip. A vector network analyzer is then used to measure the fraction of microwave power reflected from the WR-62 waveguide. Figure 3(b) shows the measured fraction of power reflected as a function of frequency, along with the expected response for two cases simulated using an FEM solver. In the first simulation case, the DRA and WR-62 are both perfectly flush with the surface of the 6 μm SiO_2 layer. In the second case, two additional air gaps are included in the simulation to account for non-idealities in the measurement setup. A small air gap G_1 between the DRA and the SiO_2 surface is included to model the uncontrolled gap in the measurement caused by surface roughness. Additionally, to avoid damaging the SiO_2 cladding during the measurement, the WR-62 was suspended just above the surface. A second air gap G_2 between the WR-62 and the SiO_2 surface is included in the simulation to account for this gap in the measurement setup. Simulations show that the value of G_1 significantly affects the resonant frequency of the DRA, while the value of G_2 primarily affects the depth of the resonance without much affect on the resonant frequency. Figure 3(b) shows excellent agreement between measurement and simulation for values of $G_1 = 2.5$ μm and $G_2 = 35$ μm. The measured resonant frequency was used to design AlN resonators with matching FSR during subsequent processing iterations.

4. AlN WAVEGUIDE DESIGN AND FABRICATION

Aluminum nitride (AlN) is an attractive material for on-chip electro-optic modulation due to its strong electro-optic response ($r_{13} \approx 1$ pm/V) and wide transparency window [28]. Additionally, AlN is a stable dielectric material suitable for applications requiring high optical power handling [29]. AlN can be sputter-deposited atop a variety of substrates in a way that results in a film which is poly-crystalline, but with a crystal axis oriented perpendicular to the substrate [30,31]. AlN can also be patterned using chlorine-based reactive ion etching (RIE) [32–34] and is generally CMOS

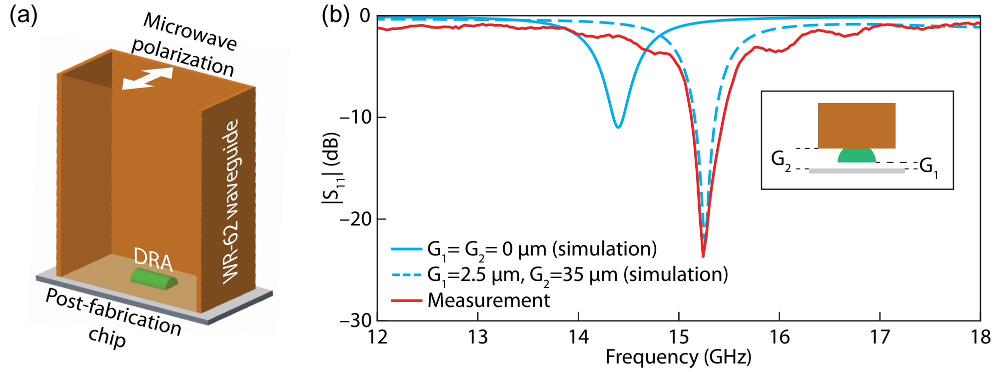

Fig. 3. (a) Schematic of the reflection measurement setup. (b) Measured $|S_{11}|$ versus frequency showing a resonance at 15.24 GHz with two simulation cases superimposed. The inset shows the locations of simulation air gaps G_1 and G_2.

process compatible. AlN ring resonators with propagation losses below 1 dB/cm have been reported [35], and AlN ring resonators have been explored for frequency comb generation [36–38], second harmonic generation [39,40], third harmonic generation [41], and electro-optic modulation [42,43]. A superconducting LC resonator was recently integrated with an AlN optical resonator for microwave-to-optical up-conversion, but this design was neither electrode-free nor did it incorporate an antenna for reception of microwave radiation [44].

Figure 4(a) shows a schematic of our waveguide cross section, consisting of an AlN waveguide with a SiO_2 cladding atop a degenerately doped Si substrate. We used a finite difference eigenmode solver to simulate the TE mode of the waveguide structure and compute the effective index of $n_{\mathrm{eff}} = 1.7$ and group index $n_g = 2.1$. Figure 4(b) shows the simulated TE mode electric field profile. The group index obtained from these simulations is used to design the circumference to match the FSR of the AlN racetrack to the expected DRA resonance of approximately 15.2 GHz.

To fabricate the AlN resonators, we thermally oxidize a degenerately doped Si wafer, forming a 2.9 µm SiO_2 buffer layer, before sputter depositing 400 nm of AlN. We then deposit a 150 nm SiO_2 layer atop the AlN via plasma-enhanced chemical vapor deposition (PECVD) to serve as a hard mask for subsequent etching. Next, we spin coat ma-N 2403 negative-tone resist, which we pattern via electron-beam lithography. The layout for the pattern was created using the CNST Nanolithography Toolbox [45]. We then transfer the pattern to the SiO_2 hard mask via flourine-based inductively coupled plasma reactive ion etching (ICP-RIE). The remaining ma-N is removed before transferring the pattern to the AlN via chlorine-based ICP-RIE. The reactive ion etching produces a sidewall angle of 75°. Finally, we deposit a 2.8 µm thick SiO_2 top cladding layer via PECVD and dice and polish the edges of the chip to allow for edge coupling of light. Figure 4(c) shows a colorized scanning electron micro-graph of the polished waveguide facet.

5. STATIC ELECTRO-OPTIC CHARACTERIZATION

Before testing the response of the device to an incident microwave excitation, we first characterize the electro-optic behavior using DC electrodes to confirm the integrity of the AlN material and measure the electro-optic coefficient r_{13}. To do so, we fabricate a smaller AlN ring resonator with an FSR of approximately 87 GHz, on top of which we pattern a gold electrode via aligned photolithography and liftoff. We then apply a DC voltage between the electrode and the Si substrate, as shown in Fig. 5(a).

In the electrostatic case, the propagation constant β of the waveguide depends on both the wavelength and applied voltage:

$$\beta = \frac{2\pi}{\lambda}\left(n_{\mathrm{eff}}(\lambda) - \frac{n_o^4 r_{13} V}{2 n_{\mathrm{eff}}(\lambda) d}\Gamma\right), \tag{19}$$

where d is the distance between the electrodes, and Γ is the dimensionless overlap integral factor [46]:

$$\Gamma \equiv \frac{d}{V}\frac{\iint_{\mathrm{core}} E_z^{\mathrm{DC}}(x,z)|\Psi(x,z)|^2 \mathrm{d}x\mathrm{d}z}{\iint |\Psi(x,z)|^2 \mathrm{d}x\mathrm{d}z}. \tag{20}$$

Figure 5(a) shows the vertical component of the electrostatic field, $E_z^{\mathrm{DC}}(x,z)$ normalized to V/d, in the region between the contacts, computed using a FEM simulation. Within the AlN core, the DC field is nearly homogeneous, with a value of $E_z^{\mathrm{DC}} = -0.52(V/d)$. Using this, together with the optical mode $\Psi(x,z)$ shown in Fig. 4(b), we calculate $\Gamma = -0.36$.

For the N-th mode of a ring resonator of length L, the propagation constant is constrained to be $\beta = 2\pi N/L$, which implies

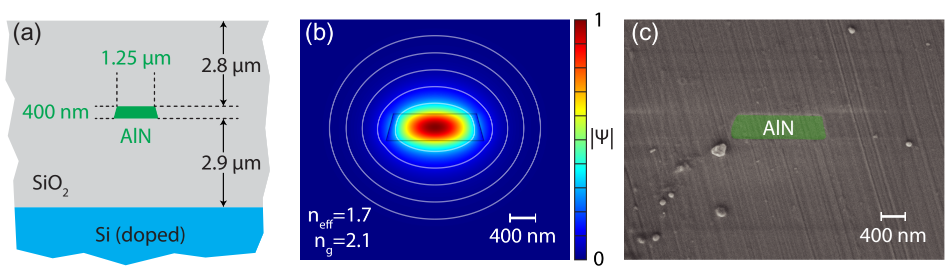

Fig. 4. (a) Cross sectional diagram of the waveguide design. (b) Transverse electric field $\Psi(x,z)$ for the fundamental quasi-TE optical eigenmode. Contour lines are separated by 10 dB. n_{eff}, effective index; n_g, group index. (c) Colorized scanning electron micrograph of the polished waveguide facet.

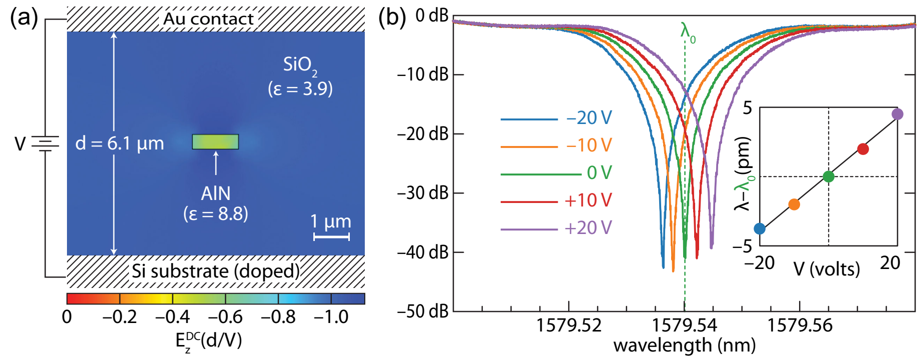

Fig. 5. (a) Electrostatic FEM simulation of the vertical electric field $E_z^{\mathrm{DC}}(x, z)$ between the electrodes, normalized to V/d. (b) Measured optical transmission of a 520 µm diameter (FSR = 87 GHz) critically coupled ring resonator for a series of applied voltages. Inset: resonance wavelength shift versus applied voltage with linear fit superimposed.

that when a voltage is applied, the resonant wavelength must shift to hold β constant. The first-order dependence of the resonant wavelength on voltage can be found by implicit differentiation of (19) with respect to V at the point ($V = 0$ V, $\lambda = \lambda_0$), which, after simplification, gives

$$\frac{d\lambda}{dV} = -\frac{n_o^4 r_{13} \lambda_0}{2 n_g n_{\mathrm{eff}} d} \Gamma, \tag{21}$$

where n_g is the group index, and λ_0 is the resonant wavelength when $V = 0$.

Figure 5(b) shows the transmission spectra of one resonance, measured for applied voltages ranging from −20 to +20 V, and the inset shows a plot of the resonant wavelength shift vs. voltage, exhibiting a slope of 0.20 pm/V. From (21), we estimate the electro-optic coefficient to be $r_{13} = 0.9$ pm/V, which agrees well with values previously reported [28].

6. RECEIVER CHARACTERIZATION

To characterize the optical and microwave performance of the receiver, we manually align the DRA to the AlN racetrack resonator. Unlike the resonator discussed in Section 5, there is no gold electrode present. A horn antenna (Pasternack PE9854-20, 20 dBi gain) suspended above the coupled chip provides the microwave excitation. Figure 6 shows a schematic and photograph of the receiver measurement setup. First, we characterize the optical performance of the AlN resonator in the absence of microwave radiation. Figure 7(a) shows the normalized optical transmission through the device as a function of optical wavelength. The resonator has a perimeter length of $L = 9369$ µm, an optical FSR of 15.2 GHz, and an extinction ratio over 20 dB indicating nearly critical coupling. By fitting the resonances in Fig. 7(a) to a Lorentzian [47], we obtain a loaded quality factor of approximately 1.1×10^5 and an intrinsic quality factor of approximately 2.2×10^5, corresponding to a propagation loss of 1.74 dB/cm. The fiber-to-fiber insertion loss of this device is approximately 15 dB, which is dominated by edge coupling to and from the lensed fibers.

Next, we characterize the receiver response to incoming microwave radiation. With our input laser tuned to the resonant wavelength near 1553.4 nm, we excite the receiver from above with 15 GHz radiation. Figure 7(b) shows the output optical spectrum depicting modulation sidebands spaced 15 GHz away from the optical carrier. The device transmission from Fig. 7(a) is superimposed to show the simultaneous alignment of the optical carrier and sidebands to three optical resonances of the device. When the microwave polarization is rotated 90° (not shown), the sidebands disappear below the noise floor, indicating the DRA is no longer resonantly excited and confirming the polarization dependence of the DRA resonant mode.

We then characterize the power in the optical sidebands as a function of microwave power, microwave frequency, optical wavelength, and microwave polarization angle. Figure 8(a) shows the sideband powers as a function of input microwave power for a fixed microwave frequency of 15.1 GHz and an optical carrier tuned to resonance. The maximum input power was limited by the output of our signal generator, and the minimum input power was chosen to ensure the output sidebands were well above the noise floor of our optical spectrum analyzer. The lines have unity slope with an intercept fit to the data, indicating a linear response.

Figure 8(b) shows the sideband powers as a function of microwave frequency for an input microwave power of 17.5 dBm

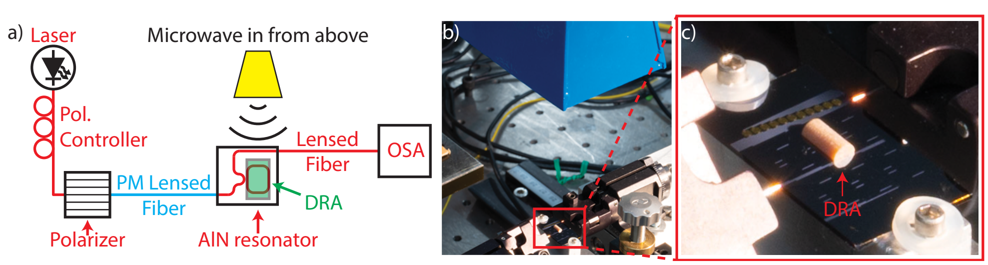

Fig. 6. (a) Schematic diagram of the measurement setup. PM, polarization maintaining; OSA, optical spectrum analyzer. (b) Photograph of the measurement setup showing the coupled chip and horn antenna. (c) Zoomed-in view of the coupled chip showing the DRA.

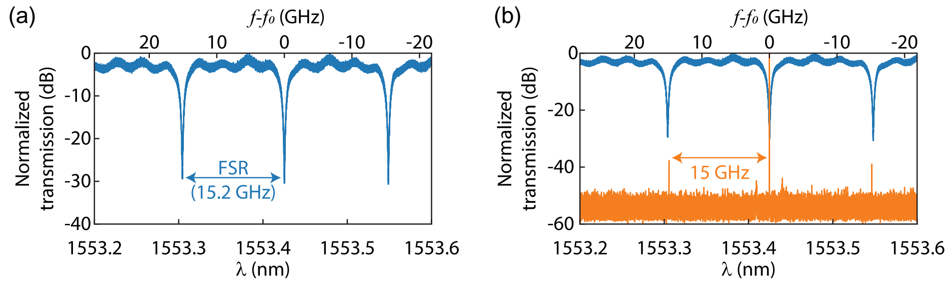

Fig. 7. (a) Normalized optical transmission through the doubly resonant device in the absence of microwave radiation as a function of optical wavelength. (b) Device output optical spectrum in the presence of resonant microwave radiation for a single resonant optical tone. The normalized optical transmission spectrum from (a) is superimposed to show the simultaneous alignment of the optical carrier and sidebands to three optical resonances of the device.

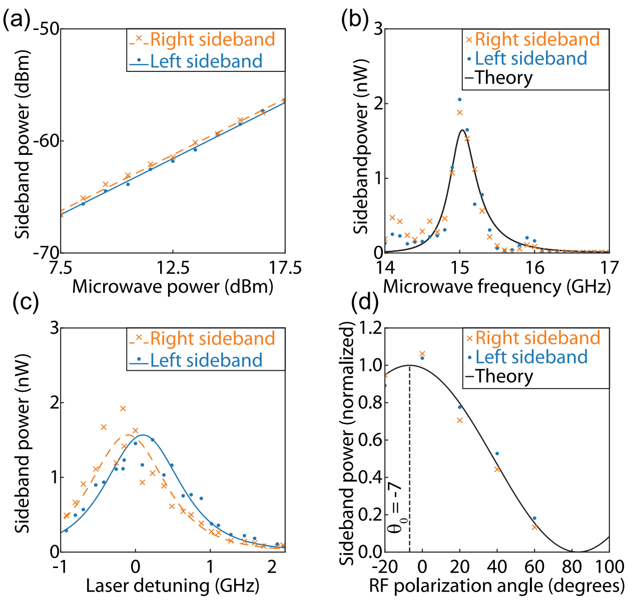

Fig. 8. (a) Optical sideband power versus microwave input power for a fixed microwave frequency of 15.1 GHz and an optical carrier that is tuned to resonance. Solid/dashed lines have unity slope with an intercept that is fit to the measured data. (b) Sideband powers as a function of microwave frequency for an input microwave power of 17.5 dBm and an optical carrier that is tuned to resonance, indicating a DRA resonance at 15 GHz. (c) Sideband powers as a function of laser detuning for a fixed microwave frequency of 15 GHz and microwave input power of 17.5 dBm. In (b) and (c) the solid/dashed lines represent the predicted response of the device from theory/simulation. The amplitude of the predicted response is scaled to fit the data. (d) Optical sideband powers versus microwave polarization angle θ in the plane of the chip for a fixed microwave frequency of 15 GHz and an optical carrier tuned to resonance. The black curve depicts the predicted response as a function of θ, with an amplitude and angle offset (θ_0) that are fit to the data. (d) is normalized to the amplitude of this predicted response.

when the optical carrier is tuned to resonance. The peak at 15 GHz corresponds to the DRA resonance.

Figure 8(c) shows the sideband powers as a function of laser detuning for a fixed microwave frequency of 15 GHz and microwave input power of 17.5 dBm. The powers are maximized when the detuning is near zero, and the slight mismatch between the left and right sideband is caused by a slight mismatch between the optical FSR of 15.2 GHz and resonant DRA microwave frequency of 15 GHz.

The lines in Figs. 8(b) and 8(c) show the theoretically predicted response and were calculated using a combination of FEM frequency domain simulation of the DRA response as a function of microwave frequency and theoretical analysis using measured values of loss, coupling, and FSR of the optical ring resonator. The FEM simulation used for these predictions is similar to that shown in Fig. 2(c), with an air gap of 2 μm introduced between the DRA and SiO_2. The thickness of the air gap was adjusted in the simulation to match the observed dielectric resonant frequency in Fig. 8(b). In both Figs. 8(b) and 8(c), the amplitude of the predicted response was scaled to fit the data. The 3 dB bandwidth of the predicted response in (b) is 430 MHz and is primarily limited by the narrower of DRA frequency response and optical wavelength response. In this case the DRA frequency response is the narrower of the two.

Figure 8(d) shows the normalized sideband powers as a function of microwave polarization angle θ within the plane of the chip for a fixed microwave frequency of 15 GHz and an optical carrier tuned to resonance. Here $\theta = 0$ corresponds to when the horn antenna is manually aligned to produce a microwave polarization perpendicular to the DRA axis. If we assume that at this frequency the contribution to the sideband powers by an electric field parallel to the DRA axis is negligible, we expect the sideband powers to have the following θ dependence:

$$P_{\mathrm{SB}} = P_0 \cos^2(\theta - \theta_0), \tag{22}$$

where P_0 is the maximum sideband power as a function of θ, and θ_0 is a parameter to allow for error in the manual alignment of the horn antenna. Both P_0 and θ_0 are fit to the data in Fig. 8(d), and P_0 is used as normalization. The black curve in Fig. 8(d) shows the result of the fit after normalization with systematic angular misalignment $\theta_0 \approx 7°$.

The minimum detectable microwave intensity depends on several factors that are intrinsic to the device, including the resonator finesse, electro-optic coefficient, microwave quality factor, and the degree of matching between the dielectric resonance and the FSR. It also depends on extrinsic factors such as the laser power, relative intensity noise, instrument dynamic range, noise floor, and spectral resolution. The intrinsic factors along with the laser power all affect the output power in the modulation sidebands according to the discussion in Sections 2 and 3. In our case, the laser power through the device was limited by the output of our tunable laser and the coupling loss to and from the lensed fibers. The other extrinsic factors listed all determine the overall noise floor of the system and are dependent on the specific measurement configuration and components used. For the measurements reported here, the minimum detectable sideband spectral intensity was observed to be −79 dBm, corresponding to the noise floor of our optical spectrum analyzer (APEX Technologies AP-2083A, 5 MHz minimum resolution bandwidth). Using the linear proportionality shown in Fig. 8(a), we estimate a corresponding minimum detectable input microwave power to be $P_{\mathrm{in}} = -5$ dBm. The intensity produced by the horn antenna is estimated as that of a symmetric diverging Gaussian beam:

$$I(z) = \frac{P_{\mathrm{in}}}{\frac{G\Lambda^2}{16\pi} + \frac{4\pi z^2}{G}}, \tag{23}$$

where P_{in} is the input microwave power, $G = 100$ (20 dBi) is the antenna gain, and $\Lambda = 2$ cm is the free-space microwave wavelength, and $z = 21$ cm is the distance from the device to the horn feed point. This yields an approximate minimum detectable microwave intensity of $I_{\mathrm{min}} = 5\ \mu\mathrm{W/cm}^2$, corresponding to a minimum detectable electric field magnitude of 6 V/m. This is an order of magnitude improvement in sensitivity over other on-chip metal-free designs [16]. The device has an on-chip footprint of 8 mm^2 and a total device thickness of 1.5 mm, amounting to a significant volume reduction when compared to similar DRA-based metal-free devices [25–27].

Table 1 shows a comparison of our device with several conductive antenna coupled electro-optic modulators from the literature. The minimum detectable E-field of our device is comparable to other devices at similar frequencies, while maintaining an entirely metal-free architecture. Additionally, while the electro-optic polymers used in several of the listed devices have very high electro-optic coefficients, they suffer from thermal and long-term stability challenges [48]. These polymers also require poling by a strong electric field produced by applying a high voltage across nearby metal electrodes on-chip. Included in this table is a prediction of our device performance for a reduced optical propagation loss of 0.5 dB/cm in the AlN. The 0.5 dB/cm prediction is based on the same theoretical analysis shown in Fig. 8(c), but with the loss parameter changed from 1.74 to 0.5 dB/cm and the coupling changed to maintain critical coupling. All other parameters remain the same. In the 0.5 dB/cm case, the minimum detectable E-field of our device is predicted to be nearly identical to that of metal antenna coupled electro-optic-polymer-based devices at similar microwave frequencies, despite AlN having an electro-optic coefficient that is two orders of magnitude weaker. Also included in this table is a prediction of our device performance at 77 GHz operating frequency, as frequencies around 77 GHz are of interest for automotive applications. The 77 GHz prediction is based on a simple scaling down of the half cylinder DRA to a radius of 0.2 mm and length of 0.8 mm, which has a resonant microwave frequency of 77 GHz in simulation. The path length of the AlN optical resonator is assumed to be scaled down so that the optical FSR matches the DRA resonant frequency, and the ring is assumed critically coupled. All other independent parameters are assumed to be the same as those measured in the 15 GHz case. The 77 GHz DRA simulation yields a peak field enhancement that is reduced by a factor of 0.55 compared to the 15 GHz case. This causes the predicted minimum detectable E-field to increase by a factor of 1.8, as seen in Table 1. Additionally, at 77 GHz the bandwidth of the DRA frequency response becomes broader than the optical wavelength response. As a result, the bandwidth of the system becomes limited by the 3 dB bandwidth of the optical resonance (1.8 GHz). It should be noted that no further optimization of this structure

Table 1. Comparison of This Work to Other Antenna Coupled Electro-Optic Modulator Designs Available in the Literature

	This Work	This Work (0.5 dB/cm Prediction)[a]	Zhang *et al.* [10]	Chung *et al.* [14]	Kanter *et al.* [15]	Park *et al.* [8]	Salamin *et al.* [13]	This Work (77 GHz Prediction)[b]
Sensitive conductive elements	N	N	Y	Y	Y	Y	Y	N
Operating frequency (GHz)	15	15	8.4	14.1	28.3	37	60	77
3 dB bandwidth (GHz)	0.43	0.36	NL	4.84	NL	2	5	1.6[c]
Device footprint (mm^2)	8	8	20.8	22.08	2	17.08	0.07	0.32
Minimum detectable E-field (V/m)	6	2	2.5	1.8	4[d]	NL	10	11[e]
Electro-optic material	AlN	AlN	SEO125 Polymer	SEO125 Polymer	$\mathrm{LiNbO_3}$	SEO125 Polymer	DLD164 Polymer	AlN
Electro-optic coefficient (pm/V)	0.9	0.9	100	135	33	100	160	0.9
Antenna type	DRA (dipole)	DRA (dipole)	Bowtie	Bowtie	Bowtie	Patch	Bowtie	DRA (dipole)

NL: Not listed.

[a]The 0.5 dB/cm prediction of our device performance is based on the same theoretical analysis shown in Fig. 8(c), but with the loss parameter changed from 1.74 to 0.5 dB/cm and the coupling changed to maintain critical coupling. All other parameters remain the same.

[b]The 77 GHz prediction is based on a simple scaling down of the half cylinder DRA to a radius of 0.2 mm and length of 0.8 mm, which has a resonant microwave frequency of 77 GHz in simulation. The path length of the AlN optical resonator is assumed to be scaled down so that the optical FSR matches the DRA resonant frequency, and the ring is assumed to be critically coupled. All other independent parameters are assumed to be the same as those measured in the 15 GHz case.

[c]The 77 GHz DRA simulation yields a peak field enhancement reduced by a factor of 0.55 compared to the 15 GHz case. This causes the predicted minimum detectable E-field to increase by a factor of 1.8.

[d]Calculated assuming a resolution bandwidth of 5 MHz.

[e]At 77 GHz, the bandwidth of the DRA frequency response becomes broader than the optical wavelength response. As a result, the bandwidth of the system becomes limited by the 3 dB bandwidth of the optical resonance (1.8 GHz).

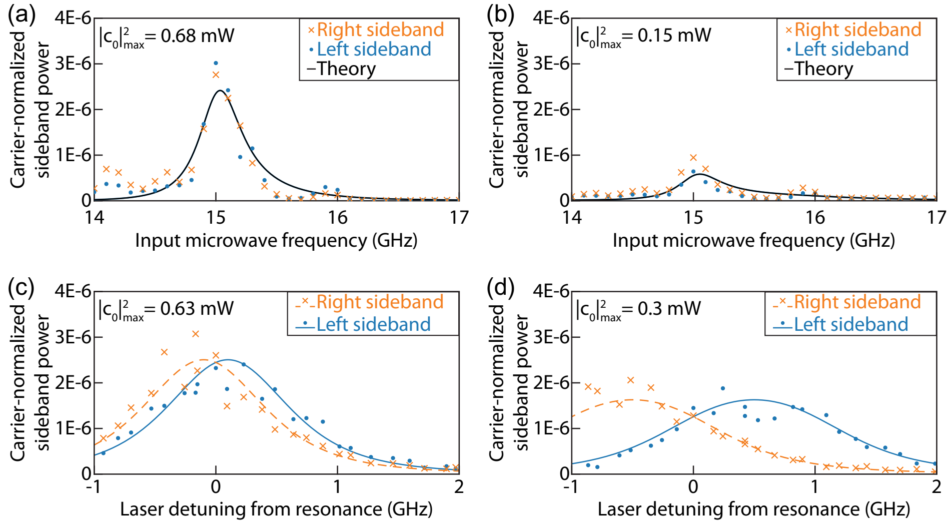

Fig. 9. (a), (b) Carrier-normalized sideband powers $|c_\pm|^2/|c_0|^2_{\mathrm{max}}$ as a function of microwave frequency for an input microwave power of 17.5 dBm and an optical carrier that is tuned to resonance for (a) the matched FSR device and (b) the unmatched FSR device. (c), (d) Carrier-normalized sideband powers $|c_\pm|^2/|c_0|^2_{\mathrm{max}}$ as a function of laser detuning for a fixed microwave frequency of 15 GHz and microwave input power of 17.5 dBm for (c) the matched FSR device and (d) the unmatched FSR device. The sideband powers are normalized to the off-resonant carrier power. In all subfigures, the solid/dashed lines represent the predicted response of the device from theory/simulation. The amplitude of the predicted response is scaled to fit the data.

was performed, so this prediction is a conservative estimate of the performance of this type of device at higher frequencies.

In Figure 9, we compare the performance of a dual-resonant device (in which the optical FSR matches the DRA resonant frequency) to that of a device with a mismatched FSR of 16 GHz. We measure the propagation loss of the second device to be 1.7 dB/cm, which is nearly identical to that of the first device. To account for differences in insertion loss, the sideband powers were normalized relative to $|c_0|^2_{\mathrm{max}}$, the optical carrier power measured when the laser was tuned far from resonance. The differences in $|c_0|^2_{\mathrm{max}}$ are primarily due to variations in edge coupling over time and across devices. Figure 9(b) shows that the mismatched device still exhibits a response at the resonant frequency of the DRA, but the relative sideband amplitude is reduced compared to the dual-resonant case shown in Fig. 9(a). Figures 9(c) and 9(d) show a similar comparison as the laser is tuned through resonance, when the microwave frequency is tuned to the DRA resonance of 15 GHz, again exhibiting a smaller response. In the mismatched case, the left and right sidebands are shifted with respect to optical detuning, because it is impossible to simultaneously match the upper and lower sidebands.

7. CONCLUSION

Here, to the best of our knowledge, we have demonstrated for the first time an entirely metal-free doubly resonant AlN electro-optic receiver for the detection of free-space microwave radiation. The doubly resonant device design allows for enhanced microwave sensitivity owing to the optical and microwave field buildup under co-resonant conditions. The bandwidth of the system is limited by the narrower of the two resonances, which in our case is the microwave DRA resonance. A DRA design with a wider bandwidth has the potential to widen the device bandwidth, albeit at the cost of sensitivity. This fully integrated on-chip microwave photonic receiver platform is scalable to higher microwave frequencies by appropriate scaling of the DRA and AlN resonant structures.

Additionally, our receiver is not limited by conductive losses found in conventional antenna and electrode structures. This opens up potential application spaces for high-frequency microwave photonics receivers, such as automotive sensing (77 GHz), satellite-based remote sensing (60 GHz), point-to-point high bandwidth communication links (up to 95 GHz), and high-band 5G (24–47 GHz). Overall, this platform is a viable on-chip metal-free alternative to standard conducting antenna-coupled electro-optic receiver designs.

Disclosures. The authors declare no conflicts of interest.

Data availability. Data underlying the results presented in this paper are not publicly available at this time but may be obtained from the authors upon reasonable request.

REFERENCES

1. C. Waldschmidt, J. Hasch, and W. Menzel, “Automotive radar—from first efforts to future systems,” IEEE J. Microw. **1**, 135–148 (2021).
2. S. S. Ahmed, “Microwave imaging in security—two decades of innovation,” IEEE J. Microw. **1**, 191–201 (2021).
3. J. Webber and M. Pospieszalski, “Microwave instrumentation for radio astronomy,” IEEE Trans. Microw. Theory Tech. **50**, 986–995 (2002).
4. F. Miranda, G. Subramanyam, F. van Keuls, *et al.*, “Design and development of ferroelectric tunable microwave components for Kuand K-band satellite communication systems,” IEEE Trans. Microw. Theory Tech. **48**, 1181–1189 (2000).
5. T. Kleine-Ostmann and T. Nagatsuma, “A review on terahertz communications research,” J. Infrared Millimeter Terahertz Waves **32**, 143–171 (2011).
6. J. C. Bardin, D. H. Slichter, and D. J. Reilly, “Microwaves in quantum computing,” IEEE J. Microw. **1**, 403–427 (2021).
7. J. Capmany and D. Novak, “Microwave photonics combines two worlds,” Nat. Photonics **1**, 319–330 (2007).
8. D. H. Park, V. R. Pagán, T. E. Murphy, *et al.*, “Free space millimeter wave-coupled electro-optic high speed nonlinear polymer phase modulator with in-plane slotted patch antennas,” Opt. Express **23**, 9464–9476 (2015).
9. H. Murata, “Millimeter-wave-band electro-optic modulators using antenna-coupled electrodes for microwave photonic applications,” J. Lightwave Technol. **38**, 5485–5491 (2020).

10. X. Zhang, A. Hosseini, H. Subbaraman, *et al.*, "Integrated photonic electromagnetic field sensor based on broadband bowtie antenna coupled silicon organic hybrid modulator," J. Lightwave Technol. **32**, 3774–3784 (2014).
11. J. Zhang, C. Luo, and Z. Zhao, "Design and application of integrated optics sensor for measurement of intense pulsed electric field," J. Lightwave Technol. **37**, 1440–1448 (2019).
12. J. Zhang, D. Yang, C. Zhang, *et al.*, "A single chip $LiNbO_3$ photonic 2D electric field sensor using two perpendicular electrodes," IEEE Photonics Technol. Lett. **32**, 1501–1504 (2020).
13. Y. Salamin, W. Heni, C. Haffner, *et al.*, "Direct conversion of free space millimeter waves to optical domain by plasmonic modulator antenna," Nano Lett. **15**, 8342–8346 (2015).
14. C.-J. Chung, X. Xu, Z. Pan, *et al.*, "Silicon-based hybrid integrated photonic chip for K_u band electromagnetic wave sensing," J. Lightwave Technol. **36**, 1568–1575 (2018).
15. G. S. Kanter, P. M. Moraw, K. F. Lee, *et al.*, "Microwave electromagnetic field sensor on thin-film lithium niobate using photonic down-conversion detection," IEEE Photonics J. **15**, 5501406 (2023).
16. S. Toroghi and P. Rabiei, "Thin film lithium niobate electric field sensors," Rev. Sci. Instrum. **93**, 034702 (2022).
17. R. K. Mongia and P. Bhartia, "Dielectric resonator antennas—a review and general design relations for resonant frequency and bandwidth," Int. J. Microw. Millim.-Wave Comput.-Aided Eng. **4**, 230–247 (1994).
18. W. Radasky, C. Baum, and M. Wik, "Introduction to the special issue on high-power electromagnetics (HPEM) and intentional electromagnetic interference (IEMI)," IEEE Trans. Electromagn. Compat. **46**, 314–321 (2004).
19. A. Han, J. Zhou, F. Du, *et al.*, "A millimeter-wave broadband reflection-less ESD protection device," IEEE Electron Device Lett. **43**, 926–929 (2022).
20. A. A. Savchenkov, A. B. Matsko, W. Liang, *et al.*, "Single-sideband electro-optical modulator and tunable microwave photonic receiver," IEEE Trans. Microw. Theory Tech. **58**, 3167–3174 (2010).
21. Q. Xu, B. Schmidt, S. Pradhan, *et al.*, "Micrometre-scale silicon electro-optic modulator," Nature **435**, 325–327 (2005).
22. A. Rueda, F. Sedlmeir, M. C. Collodo, *et al.*, "Efficient microwave to optical photon conversion: an electro-optical realization," Optica **3**, 597–604 (2016).
23. V. S. Ilchenko, A. A. Savchenkov, A. B. Matsko, *et al.*, "Whispering-gallery-mode electro-optic modulator and photonic microwave receiver," J. Opt. Soc. Am. B **20**, 333–342 (2003).
24. G. Santamaría Botello, F. Sedlmeir, A. Rueda, *et al.*, "Sensitivity limits of millimeter-wave photonic radiometers based on efficient electro-optic upconverters," Optica **5**, 1210–1219 (2018).
25. R. C. J. Hsu, A. Ayazi, B. Houshmand, *et al.*, "All-dielectric photonic-assisted radio front-end technology," Nat. Photonics **1**, 535–538 (2007).
26. A. Ayazi, R. C. J. Hsu, B. Houshmand, *et al.*, "All-dielectric photonic-assisted wireless receiver," Opt. Express **16**, 1742–1747 (2008).
27. A. A. Savchenkov, W. Liang, V. S. Ilchenko, *et al.*, "Photonic E-field sensor," AIP Adv. **4**, 122901 (2014).
28. S. Zhu and G.-Q. Lo, "Aluminum nitride electro-optic phase shifter for backend integration on silicon," Opt. Express **24**, 012501 (2016).
29. X. Liu, A. W. Bruch, and H. X. Tang, "Aluminum nitride photonic integrated circuits: from piezo-optomechanics to nonlinear optics," Adv. Opt. Photonics **15**, 236–317 (2023).
30. A. Stolz, A. Soltani, B. Abdallah, *et al.*, "Optical properties of aluminum nitride thin films grown by direct-current magnetron sputtering close to epitaxy," Thin Solid Films **534**, 442–445 (2013).
31. E. Dogheche, D. Rémiens, A. Boudrioua, *et al.*, "Growth and optical characterization of aluminum nitride thin films deposited on silicon by radio-frequency sputtering," Appl. Phys. Lett. **74**, 1209–1211 (1999).
32. X. Liu, C. Sun, B. Xiong, *et al.*, "Smooth etching of epitaxially grown AlN film by Cl2/BCl3/Ar-based inductively coupled plasma," Vacuum **116**, 158–162 (2015).
33. V. Bliznetsov, B. H. B. Johari, M. T. Chentir, *et al.*, "Improving aluminum nitride plasma etch process for MEMS applications," J. Micromech. Microeng. **23**, 117001 (2013).
34. A. P. Shah, A. Azizur Rahman, and A. Bhattacharya, "Temperature-dependence of Cl_2/Ar ICP-RIE of polar, semipolar, and nonpolar GaN and AlN following BCl_3/Ar breakthrough plasma," J. Vac. Sci. Technol. A **38**, 013001 (2020).
35. S. Zhu, Q. Zhong, T. Hu, *et al.*, "Aluminum nitride ultralow loss waveguides and push-pull electro-optic modulators for near infrared and visible integrated photonics," in *Optical Fiber Communication Conference (OFC)* (OSA, 2019), paper W2A.11.
36. H. Jung, K. Y. Fong, C. Xiong, *et al.*, "Electrical tuning and switching of an optical frequency comb generated in aluminum nitride microring resonators," Opt. Lett. **39**, 84–87 (2014).
37. H. Jung and H. X. Tang, "Aluminum nitride as nonlinear optical material for on-chip frequency comb generation and frequency conversion," Nanophotonics **5**, 263–271 (2016).
38. Z. Gong, A. Bruch, M. Shen, *et al.*, "High-fidelity cavity soliton generation in crystalline AlN micro-ring resonators," Opt. Lett. **43**, 4366–4369 (2018).
39. J. B. Surya, X. Guo, C.-L. Zou, *et al.*, "Control of second-harmonic generation in doubly resonant aluminum nitride microrings to address a rubidium two-photon clock transition," Opt. Lett. **43**, 2696–2699 (2018).
40. A. W. Bruch, X. Liu, X. Guo, *et al.*, "17 000%/W second-harmonic conversion efficiency in single-crystalline aluminum nitride microresonators," Appl. Phys. Lett. **113**, 131102 (2018).
41. J. B. Surya, X. Guo, C.-L. Zou, *et al.*, "Efficient third-harmonic generation in composite aluminum nitride/silicon nitride microrings," Optica **5**, 103–108 (2018).
42. C. Xiong, W. H. P. Pernice, and H. X. Tang, "Low-loss, silicon integrated, aluminum nitride photonic circuits and their use for electro-optic signal processing," Nano Lett. **12**, 3562–3568 (2012).
43. B. Dong, Q. Shi, T. He, *et al.*, "Integration of aluminum nitride modulator and textile triboelectric nanogenerator toward self-sustainable tunable wearable photonics," in *IEEE 33rd International Conference on Micro Electro Mechanical Systems (MEMS)* (2020), pp. 1234–1237.
44. W. Fu, M. Xu, X. Liu, *et al.*, "Cavity electro-optic circuit for microwave-to-optical conversion in the quantum ground state," Phys. Rev. A **103**, 053504 (2021).
45. K. C. Balram, D. A. Westly, M. Davanco, *et al.*, "The nanolithography toolbox," J. Res. Natl. Inst. Stand. **121**, 464–475 (2016).
46. C. Kim and R. Ramaswamy, "Overlap integral factors in integrated optic modulators and switches," J. Lightwave Technol. **7**, 1063–1070 (1989).
47. T. Christopoulos, O. Tsilipakos, G. Sinatkas, *et al.*, "On the calculation of the quality factor in contemporary photonic resonant structures," Opt. Express **27**, 14505–14522 (2019).
48. M. Wang, Y. Chen, S. Zhang, *et al.*, "Perspectives of thin-film lithium niobate and electro-optic polymers for high-performance electro-optic modulation," J. Mater. Chem. C **11**, 11107–11122 (2023).